FULL PAPER

In Situ Study of Nanostructure and Electrical Resistance of Nanocluster Films Irradiated with Ion Beams

Weilin Jiang, Jennifer A. Sundararajan, Tamas Varga, Mark E. Bowden, You Qiang, John S. McCloy, Charles. H. Henager Jr., and Robert O. Montgomery*

An in situ study is reported on the structural evolution in nanocluster films under He^+ ion irradiation using an advanced helium ion microscope. The films consist of loosely interconnected nanoclusters of magnetite or iron-magnetite (Fe-Fe_3O_4) core-shells. The nanostructure is observed to undergo dramatic changes under ion-beam irradiation, featuring grain growth, phase transition, particle aggregation, and formation of nanowire-like network and nanopores. Studies based on ion irradiation, thermal annealing and electron irradiation have indicated that the major structural evolution is activated by elastic nuclear collisions, while both electronic and thermal processes can play a significant role once the evolution starts. The electrical resistance of the Fe-Fe_3O_4 films measured in situ exhibits a super-exponential decay with dose. The behavior suggests that the nanocluster films possess an intrinsic merit for development of an advanced online monitor for fast neutron radiation with both high detection sensitivity and long-term applicability, which can enhance safety measures in many nuclear operations.

1. Introduction

Among all sources of near-zero carbon-emission energies, nuclear energy is the only available, proven and affordable large-power electricity generation to date.[1] According to recent reports,[2] nearly 15% of the electricity needs worldwide were provided by nuclear power plants, and even larger percentages in France (80%) and US (20%). With increasing demand for electricity, nuclear energy must be one of the essential parts in the diversity of energy sources, especially at the current stage of underdeveloped renewable energy. New nuclear power plants are being built and more are planned over the next decades.[2] However, severe nuclear accidents[3] that occurred in Three Mile Island, US (1979), Chernobyl, USSR (1986), and more recently in Fukushima, Japan (2011) have decreased the public confidence of using nuclear power, which greatly underscores the importance of meeting the highest standards of safety, both in operation of the existing nuclear power plants and in new designs of advanced nuclear reactors, including small modular reactors.[4] To date, many of the existing reactors are approaching their designed operation lifetime. As a priority, research is critically needed to develop technologies that will sustain the safety of current reactors, including advanced monitoring systems that can quantify the "state of health" of structural materials in the current reactor fleet and predict their residual safe operating life. In addition, the monitoring system can be integrated into advanced reactors and new builds for inspectability and safety enhancement. Fast neutron monitors have been developed for application in various fields, including a spallation neutron source,[5] material testing reactors,[6] a subcritical facility,[7] and an accelerator-based neutron generator.[8] Many of the designs involve a coating of polyethylene[5,7,9] or fissile materials,[6] interacting with fast neutrons to create proton recoils or fission products that ionize gas and form electrical signals. In nuclear plants and neutron irradiation facilities, small online fast neutron flux monitors are much needed for effective assessment of material degradation in critical areas as well as for measurement of fast neutron dose in irradiated samples.

Nanostructured materials are of both scientific interest and technological importance.[10] Their potential as an advanced sensing material for nuclear radiation has not been extensively explored. So far, very few reports have been published in the research field. Our previous studies[11] indicate that highly porous films of loosely interconnected magnetite (Fe_3O_4) nanoclusters, composed of crystalline grains of ~3 nm in size, undergo a dramatic change in nanostructure after 5.5 MeV Si^{2+} ion irradiation to a fluence of 10^{16} Si^{2+}/cm^{-2} at nominally room temperature (RT). The structural change leads to magnetic domain growth, occurrence of magnetic anisotropy, and transition from superparamagnetic to ferromagnetic behavior. Similar as-deposited films of $SmCo_5$ nanoparticles with an average size of 3.5 nm were also shown to be superparamagnetic.[12] Recently, nanocluster films of iron-magnetite (Fe-Fe_3O_4) core-shells were found[13] to reduce Fe valence in the oxide shell after ion irradiation. In general, energy deposition by ion irradiation

Dr. W. Jiang, Dr. T. Varga, Dr. M. E. Bowden, Dr. C. H. Henager Jr., R. O. Montgomery
Pacific Northwest National Laboratory
Richland, WA 99352, USA
E-mail: weilin.jiang@pnnl.gov
J. A. Sundararajan, Prof. Y. Qiang
University of Idaho
Moscow, ID 83844, USA
Prof. J. S. McCloy
School of Mechanical and Materials Engineering
Washington State University
Pullman, WA 99164, USA

DOI: 10.1002/adfm.201400553

modifies material structure and properties through defect generation, accumulation and interaction, amorphization, phase transition, nucleation and growth of precipitates and gas blisters, grain growth, void formation, volumetric expansion, micro-cracking, etc. Material resistance or susceptibility to nuclear radiation depends on its structural stability. It is crucial to study structural changes induced by nuclear irradiation and, in particular, evolution of nanostructures examined by in situ methods that produce data capable of gaining physical insights into the basic processes involved in the structural changes. Previous in situ studies of microstructural evolution under ion irradiation have employed a transmission electron microscope (TEM) interfaced with an ion implanter or accelerator,[14] including facilities at Argonne National Laboratory in US,[15] National Institute for Materials Science in Japan,[16] Center of Nuclear Spectrometry and Mass Spectrometry in France,[17] Wuhan University in China,[18] and more recently at Sandia National Laboratory,[19] to just list a few. By using the in situ capabilities over the past decades, major advances have been achieved in understanding defect formation, defect interactions and nanostructural evolution in various ion-beam irradiated materials.[15,20] Other in situ methods have also been developed and applied to study behavior of battery materials under different conditions.[21]

One focus of this study is the in situ examination of nanostructural evolution with dose in nanocluster films of Fe_3O_4 and Fe-Fe_3O_4. Recent technological advances have led to emergence of Helium Ion Microscope (HIM).[22] Compared to conventional Scanning Electron Microscope (SEM), HIM has demonstrated an improved imaging capability with better surface sensitivity, higher spatial resolution, larger depth of field, and sharper atomic number contrast. Since its commercialization in 2007, HIM has produced impactful results in a number of fields, including precision graphene cutting,[23] imaging of nanostructures and biological samples,[11,24] patterning and lithography,[25] and elemental analysis with sub-nanometer spatial resolution.[26] While imaged using secondary electrons or backscattered He^+ ions, the material is simultaneously under He^+ ion irradiation, which produces atomic displacements in the material. This unique characteristic allows HIM to be applied to in situ study of nanostructural evolution under He^+ ion irradiation at sub-nanometer resolution (0.35 nm) within the beam dwelling time, typically on the order of tens to hundreds of microseconds per pixel. It should be noted that under normal operation conditions, HIM provides high-quality imaging with negligible damage production. Very high ion fluence must be applied for most materials in order to produce observable morphology changes on the surface. Subsurface lattice damage from energetic He^+ ions can be investigated through cross-sectional view.[27] Compared to the TEM-accelerator system, HIM provides a new, complementary in situ capability for studying bulk samples. Some samples (e.g., nanocluster films in this study) that are not very convenient to study under TEM may be examined in situ using HIM with a comparable spatial resolution.

The other focus of this study is the in situ measurement of the electrical resistance of nanocluster films irradiated with accelerator-generated MeV ions using van der Pauw method.[28] This method is particularly effective for samples whose electrical resistance decreases with increasing dose. Measurements of such samples will not lead to a higher leak current through the substrate at a higher dose, which would otherwise have a larger experimental error. In contrast to a dramatic increase in the electrical resistivity of many metals and ceramics, including Al, Cu and Si upon irradiation due to defect accumulation,[29] our preliminary tests showed a significant decrease in the electrical resistance of a nanocluster film after ion irradiation. This behavior makes the films attractive as candidate sensing materials for irradiation study of electrical resistance.

2. Results and Discussion

2.1. Structural Evolution in Fe_3O_4 Nanocluster Film

An in situ study of structural evolution in a magnetite Fe_3O_4 nanocluster film on a surface-oxidized Si substrate at nominally RT has been performed under 25 keV He^+ ion irradiation using HIM. According to the full-damage cascade simulation based on the Stopping and Range of Ions in Matter (SRIM) code,[30] where the threshold displacement energy for each of the sublattices in Fe_3O_4 is assumed to be 25 eV in this study, atomic displacement rate is estimated to be ~0.26 displ./nm/ion at the surface and ~0.64 displ./nm/ion at the damage peak that is located at the depth of ~120 nm (assuming the theoretical specific gravity of 5.197 g/cm^3 and hereafter) (Figure S1). It should be noted that these assumptions are not accurate, which affect the absolute values of dose in displacements per atom (dpa) and the length (nm) in a linear scale, but do not have major impact on the data interpretation in this study. The sputtering rate under the irradiation conditions is predicted to be negligible; the electronic and nuclear stopping powers at the surface correspond to 139 and 12 keV/μm, respectively. In this study, a local dose in displacements per atom (dpa) at the surface is estimated for HIM examination, and an average dose in dpa over the entire film thickness for grazing-angle incidence x-ray diffraction (GIXRD) and electrical resistance measurement. In all events of this study, the film thickness is much smaller than the ion projected range so that a great majority of ions penetrated the nanocluster films.

Three HIM images of the surface nanostructures of the Fe_3O_4 nanocluster film are shown in **Figure 1** at ion fluences of 3.3×10^{16}, 7.6×10^{17} and 1.9×10^{18} He^+/cm^2, corresponding to doses of 0.9, 20 and 51 dpa at the surface, respectively, with a dose rate of ~8.5×10^{-3} dpa/s. Apparently, with increasing dose, nanoclusters aggregate to form larger particles, resulting in formation of a nanowire-like network accompanied by nano-pores. A movie (Movie S1) with 30 image frames has been made from the in situ HIM examination, which is available in the online supporting information. The movie clearly demonstrates nanostructural evolution with increasing dose. Upon irradiation, the loosely interconnected nanoparticles tend to aggregate. With increasing dose, small particles are absorbed by larger ones, resulting in an overall increase in the particle size. Larger particles interconnect themselves and gradually form a nanowire-like network with concurrent formation of nano-pores. Previous GIXRD for a 2 μm thick Fe_3O_4 nanocluster film irradiated

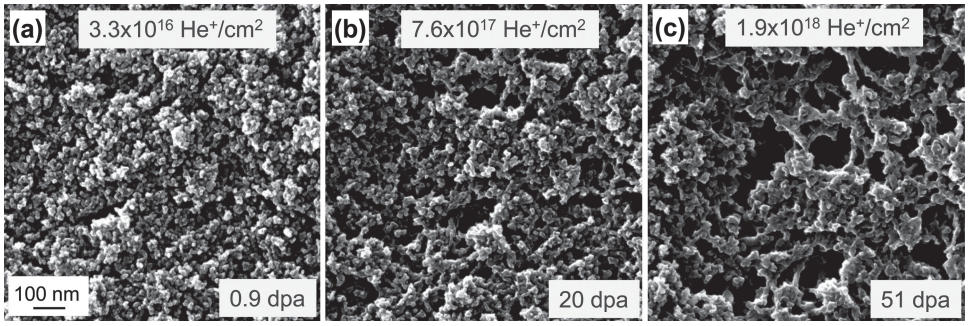

Figure 1. Selected HIM (operating at 25 kV) snapshots of a nanocluster magnetite Fe_3O_4 film on a surface-oxidized Si substrate irradiated to various ion fluences: (a) 3.3×10^{16}, (b) 7.6×10^{17} and (c) 1.9×10^{18} He^+/cm^2 at nominally RT. The images have the same scalar bar and show a significant change in the nanostructure (same area).

to a fluence of 10^{16} Si^{2+}/cm^2, or an average dose of ~4 dpa in the film, indicates[11] a significant increase in grain size. Grain growth takes place at the expense of the surrounding amorphous material through irradiation-induced epitaxy at the interface and/or by coalescence of neighboring nano-grains. Each grain is a single-domain magnet; irradiation-assisted reorientation of their magnetic moments could provide at least part of the driving force for the coalescence to occur.

Irradiation with energetic ions provides three major stimuli to induce nanostructural changes: nuclear elastic collision-induced atomic displacements, electronic energy deposition-induced atomic excitation and ionization, and heat production-induced thermal processes. Experiments were designed and performed to study the individual contributions of these three processes. While He^+ irradiation was conducted at nominally RT, the temperature within the beam spot is expected to be higher than RT. The actual temperature within the beam spot depends on ion energy, flux, material thermal conductivity, etc. Accurate measurement of the temperature within the small beam spot (1 μm × 1 μm) was not possible in the HIM. Calculations[31] also have formidable challenges because of the porous nature and structural evolution. Irradiation of a similar Fe_3O_4 nanocluster film at nominally RT with 5.5 MeV Si^{2+} ions at a flux of ~10^{12} $Si^{2+}/cm^2/s$ indicated[11] a temperature increase of less than 50 K near the large beam spot (12.5 mm × 12.5 mm) on the surface. To study thermal effects on the nanostructural evolution, the as-deposited Fe_3O_4 nanocluster film used in Figure 1 was cleaved to four smaller samples; two of them were annealed in flowing Ar gas environments at 473 and 773 K, respectively, for 10 hours each. **Figure 2** shows the surface nanostructures in different areas on the film surface before and after the thermal annealing steps. The data in Figure 2 do not suggest a noticeable modification in the nanostructure after the thermal treatments at temperatures up to 773 K.

In situ electron irradiation was also carried out for one of the as-cleaved samples using an SEM operating at a voltage of 20 kV and a high electron beam current of 0.96 nA. At the electron energy of 20 keV, permanent atomic displacements cannot be produced in Fe_3O_4 crystal due to the limited kinetic energy transferred from the electrons to target atoms (maximum of ~3 eV to ^{16}O and of ~0.8 eV to ^{56}Fe) in the elastic collision process, which is well below the threshold displacement energy (presumably on the order of tens of eV.[32] The primary electrons lose their energy in the material mainly through excitation and ionization of the target atoms with multiple interactions. As a result, secondary electrons, photons, and phonons are generated in the electron energy loss process. It should be noted that the electronic energy deposition can influence kinetic process by increasing the sample temperature and modifying energy barriers for diffusion. **Figure 3** shows three SEM micrographs of the Fe_3O_4 nanocluster film used in Figure 1 before and after electron irradiation to 4.4×10^{19}, 1.3×10^{21} and 2.6×10^{21} e/cm^2 at nominally RT. Although the SEM images have a worse resolution and a weaker contrast compared to the HIM images, they provide clear evidence that the nanostructure at the surface of the nanocluster film does not change noticeably up to 2.6×10^{21} e/cm^2. This behavior is also clearly demonstrated in a movie (Movie S2) in the online supporting information.

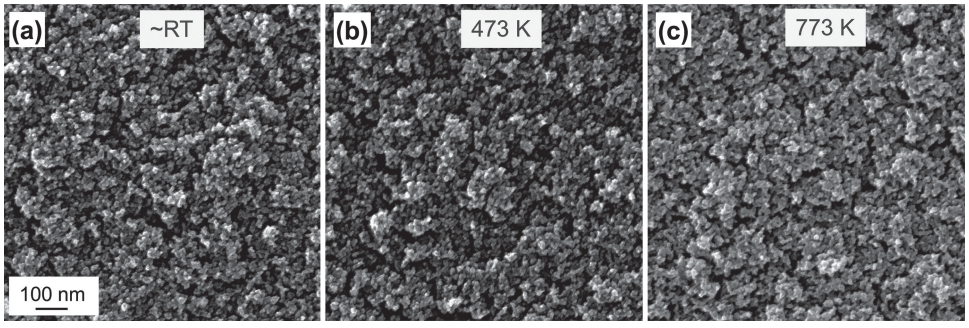

Figure 2. HIM (operating at 25 kV) micrographs of the same nanocluster magnetite Fe_3O_4 film in Figure 1: (a) as-deposited at nominally RT, (b) annealed at 473 K and (c) at 773 K for 10 hours each in flowing Ar gas environments. The images have the same scalar bar and show a similar nanostructure (different areas).

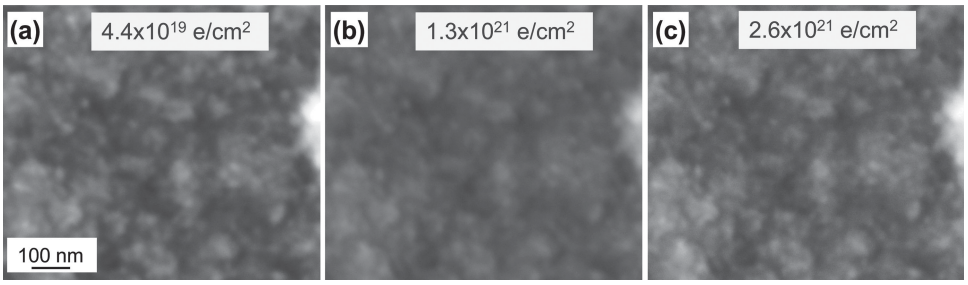

Figure 3. Selected SEM (operating at 20 kV) snapshots of the same nanocluster magnetite Fe_3O_4 film in Figure 1, irradiated to various electron fluences: (a) 4.4×10^{19}, (b) 1.3×10^{21} and (c) 2.6×10^{21} e/cm^2 at nominally RT. The images have the same scalar bar and show a similar nanostructure (same area).

The density of the electronic energy deposition ρ_e is the product of ion/electron fluence F and electronic stopping power $(dE/dx)_e$:

$$\rho_e = F \times \left(dE/dx\right)_e \quad (1)$$

Similarly, the rate of the electronic energy deposition γ_e is the product of ion/electron flux f and $(dE/dx)_e$:

$$\gamma_e = f \times \left(dE/dx\right)_e \quad (2)$$

According to the National Institute of Standards and Technology (NIST) ESTAR database,[33] the electronic stopping powers of 20 keV electrons in Fe and O are 8.468 and 11.38 MeV cm^2/g, respectively. Based on Bragg's rule,[34] the electronic stopping power of the electrons in Fe_3O_4 is estimated to be 10.13 MeV cm^2/g. Similarly, using ASTAR database,[33] the electronic stopping power for 25 keV He^+ ions in Fe_3O_4 is 412.8 MeV cm^2/g. As a rough estimation, Equation (1) gives a density ratio $[\rho_e(e)/\rho_e(He^+)]$ of ~30 based on 20 keV electron irradiation to 2.6×10^{21} e/cm^2 and 25 keV He^+ ion irradiation to 1.9×10^{18} He^+/cm^2. This indicates a significantly higher energy density deposited by the electrons (Figure 3c) than by the He^+ ions (Figure 1c) at the surface. From Equation (2), the rate ratio $[\gamma_e(e)/\gamma_e(He^+)]$ for the electron irradiation (0.96 nA over an area of 2.5 μm × 2.3 μm) and He^+ ion irradiation (0.5 pA over 1 μm × 1 μm) is ~8, which suggests that the local temperature at the surface within the beam spot of the electrons in SEM should be higher than that of the He^+ ions in HIM. In a sharp contrast to a significant change in the nanostructure induced by He^+ ions (Figure 1c), electron irradiation does not suggest an observable change up to the highest fluence of 2.6×10^{21} e/cm^2 in spite of the considerably larger values of $\rho_e(e)$ and $\gamma_e(e)$ compared to $\rho_e(He^+)$ and $\gamma_e(He^+)$, respectively. The result from Figure 3 indicates that the combined effects from the electronic energy deposition and the beam heating are not a major contributor to activate observable structural evolution in the Fe_3O_4 nanocluster film.

Because both thermal and electronic processes can hardly alter the structure of the Fe_3O_4 nanocluster film, nuclear elastic collision is concluded to be primarily responsible for the activation of the dramatic nanostructural evolution at high doses. It should be noted that despite their inactivity for observable structural change, both thermal and electronic processes can play a significant role once the nanostructural evolution starts. They can also induce local atomic rearrangements and minor modifications in the nanostructure without nuclear collisions. The results from Figure 1 to 3 suggest that the structure of the nanocluster films is likely to be susceptive to fast neutron irradiation, where the first-order electronic process is absent, but both atomic displacements and heat production processes are active. Because of a much smaller energy transfer that hardly produces displaced atoms in the films, activation of major nanostructural evolution by electrons or gamma-rays from nuclear decays is improbable.

2.2. Nanostructural Evolution and Phase Transition in Fe-Fe_3O_4 Core-Shell Nanocluster Film

Figure 4 shows the surface structures of a Fe-Fe_3O_4 core-shell nanocluster film on a surface-oxidized Si irradiated with

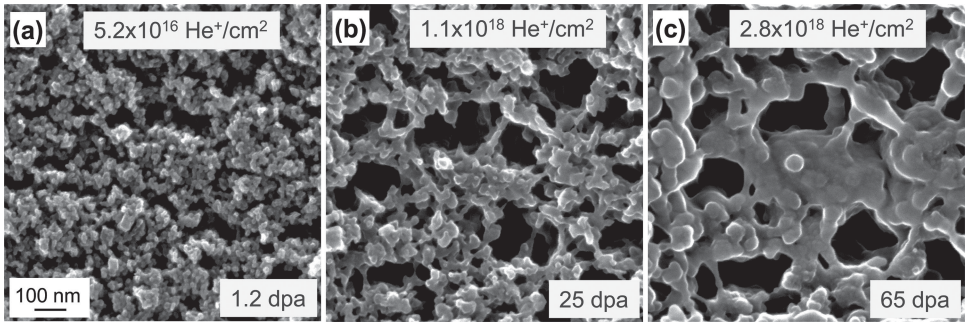

Figure 4. Selected HIM (operating at 30 kV) snapshots of a Fe-Fe_3O_4 core-shell nanocluster film on a surface-oxidized Si substrate irradiated to various ion fluences: (a) 5.2×10^{16}, (b) 1.1×10^{18} and (c) 2.8×10^{18} He^+/cm^2 at nominally RT. The images have the same scalar bar and show a dramatic change in the nanostructure (same area).

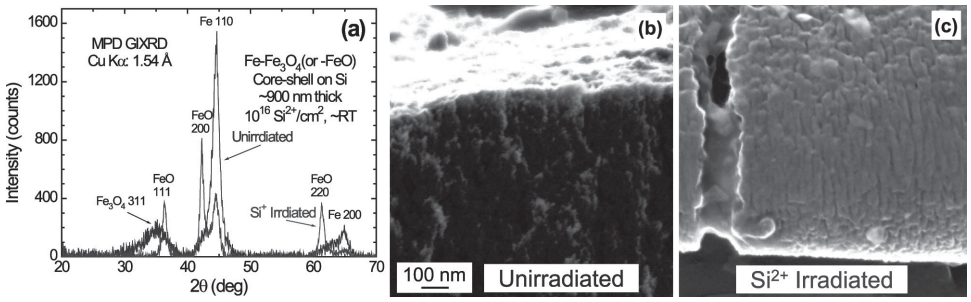

Figure 5. (a) Background subtracted GIXRD patterns for a Fe-Fe_3O_4 core-shell nanocluster film on Si before and after 5.5 MeV Si^+ ion irradiation to 10^{16} Si^+/cm^2 (~0.95 dpa in the film and ~0.53 dpa at the surface) at nominally RT. Also shown are the corresponding cross-sectional HIM images of the film (b) before and (c) after the irradiation. The two images have the same scalar bar.

30 keV He^+ ions to 5.2×10^{16}, 1.1×10^{18} and 2.8×10^{18} He^+/cm^2 at nominally RT, corresponding to 1.2, 25 and 65 dpa at the surface, respectively. The nanoclusters have a Fe core of ~8 nm in diameter and a Fe_3O_4 shell of ~2 nm in thickness. Typical TEM micrographs showing the nanoclusters, nanograins and core-shell structure are provided in the supporting information (Figure S2). As an approximation for the core-shell structure, magnetite Fe_3O_4 was used for SRIM[30] simulation. The results (Figure S1) indicate that the atomic displacement rate and electronic stopping power at the surface are 0.22 displ./nm/ion and 155 keV/μm, respectively, which are comparable to those from 25 keV He^+ ion irradiation of Fe_3O_4. Similar to the structural evolution in the Fe_3O_4 nanocluster film shown in Figure 1, loosely interconnected small particles in the Fe-Fe_3O_4 core-shell nanocluster film aggregate to form larger particles as dose increases, followed by formation of a nanowire-like network with nano-pores. A movie file (Movie S3) in the supporting information shows that with increasing dose, the nanostructure shrinks gradually till the dose reaches to 45 dpa at the surface (or an ion fluence of 2×10^{18} He^+/cm^2), where the structure begins to expand in volume, including the agglomerated nanoparticle at the image center. The resulting surface morphology resembles that of a similar core-shell film after irradiation with Si^{2+} ions, where phase transition of the oxide shell was observed (see below). This volumetric expansion is not yet understood at this stage, but might be associated with helium accumulation, phase transition, defect-induced swelling, combination of those or other processes. Further studies are needed for clarification.

To study possible changes in crystal phase and grain size, a 3.0 MV ion accelerator was used for a larger-area irradiation that covers the entire surface area of a Fe-Fe_3O_4 core-shell nanocluster film [~900 nm in thickness determined by Rutherford backscattering spectrometry (RBS)]. The irradiation was performed with 5.5 MeV Si^{2+} ions at nominally RT in the low vacuum range of 10^{-7} Torr to a fluence of 10^{16} Si^{2+}/cm^2, corresponding to an average dose of ~0.95 dpa in the film thickness. **Figure 5**a shows the GIXRD pattern for the film before and after irradiation. The results from the whole-pattern fitting indicate that prior to irradiation, the crystalline grains consisted of a Fe core of 8 nm in diameter with a shell Fe_3O_4 of 2 nm in thickness on the average. After irradiation, the average size of the Fe core decreased slightly to 7 nm; the oxide shell transformed from cubic magnetite Fe_3O_4 to cubic wüstite FeO with the average shell thickness increased to 13 nm. The weight ratio of Fe in the film decreased from 81% to 36%. The physical processes involved in the structural evolution can be complex and are not clear at this time, but they might include creation of O interstitials in Fe_3O_4 by ion irradiation, followed by O migration, oxidation of Fe atoms, and phase transition (probably due to oxygen vacancy accumulation) to cubic FeO in the shell under the irradiation conditions. Further irradiation-assisted epitaxial growth of FeO at the amorphous/crystalline interface cannot be ruled out. Obviously, cubic wüstite is the preferred phase over the cubic magnetite for the oxide shell on a Fe core under the irradiation conditions. This observation is consistent with the literature reports. Similar behavior of Fe valence reduction in the shell of a Fe-Fe_3O_4 nanocluster film was also observed after ion irradiation.[13] A previous study[35] has indicated that a large fraction of nanophase FeO can be grown on sapphire when the growth rate is high. Although wüstite is known as a high-pressure phase,[36] thin epitaxial FeO films on Fe have been found to be stable even in vacuum at RT.[37] The cross-sectional view of the film nanostructures before and after Si^{2+} ion irradiation is shown in Figure 5b and 5c, respectively. As a result of the irradiation, the highly porous film becomes a columnar structure that is aligned with the irradiation direction (surface normal). Nano-cracks in the irradiated film also appear, as shown in Figure 5c, which could be attributed to accumulation and redistribution of nano-pores that are formed during ion irradiation, similar to those observed in Figure 4.

2.3. Response of Fe-Fe_3O_4 Nanocluster Film Resistance to Ion Irradiation

In situ electrical resistance measurements of Fe-Fe_3O_4 core-shell nanocluster films irradiated with 5.5 MeV Si^{2+} and 2.0 MeV He^+ ions at nominally RT and 473 K have been performed based on van der Pauw four-probe method.[28] The behavior of the resistance changes from the reciprocal measurements along the horizontal and vertical directions has been found to be similar in this study and only vertical average resistance is shown and discussed in this report. **Figure 6** shows the average resistance of a 200 nm thick Fe-Fe_3O_4 nanocluster film at nominally RT as a function of Si^{2+} ion fluence (bottom axis) and average dose in the film (top axis). The in situ result suggests that under the ion irradiation there is a super-exponential decay dependence of the electrical resistance on dose in the Fe-Fe_3O_4 nanocluster film.

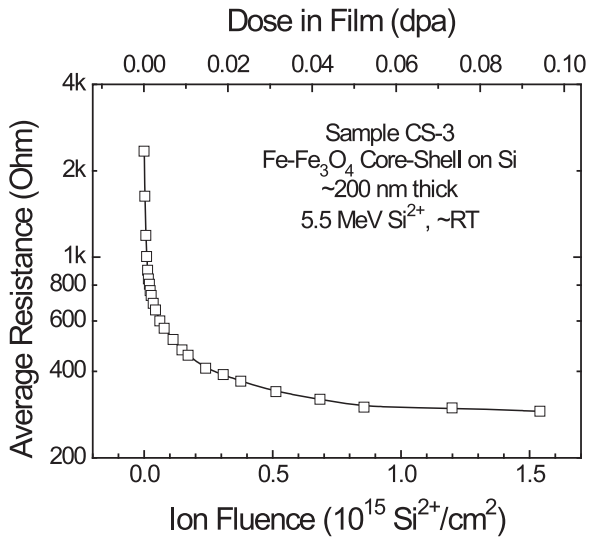

Figure 6. Electrical resistance of a Fe-Fe_3O_4 core-shell nanocluster film on surface-oxidized Si measured in situ using van der Pauw method as a function of ion fluence during 5.5 MeV Si^{2+} ion irradiation at nominally RT. A super exponential decay behavior of the resistance is observed.

The electrical resistance decreases from ~2.3 kΩ for the as-deposited film to ~290 Ω at a dose of ~0.09 dpa. The resistance in the entire dose range is much smaller than that of the blank substrate (without film), which has a value of ~10 MΩ with a weak dependence on dose. Thus, the leak current through the substrate is negligible at all doses in the measurement. The resistance behavior shown in Figure 6 suggests that the nanocluster film has potential as a sensing material for monitoring of nuclear radiation, including neutron flux as discussed above. The relative change in the electrical resistance with dose is associated with the flux. In the low-dose regime (<0.01 dpa), the material is extremely susceptible to nuclear radiation, providing potential for high-sensitivity detection. The resistance decreases more gradually in the higher-dose regime, allowing for a possible long-term use. It should be noted that there could be a significant reduction in the electrical resistance by ion irradiation prior to a dramatic nanostructural change that occurs at higher doses (see below).

The surface morphologies of the in situ sample used in Figure 6 before and after irradiation are shown in **Figure 7**. At the final fluence of ~1.5×10^{15} Si^{2+}/cm^2 (or 0.08 dpa at the surface), a dramatic change in the nanostructure (irradiated at nominally RT) is exhibited, featuring nanocluster aggregation and nano-pore formation. The overall nanostructure is similar to that of the agglomerated nanoparticle at the image center of Figure 4c, resulted from He^+ ion irradiation of a similar core-shell film to 65 dpa at the surface, about 800 times higher than the dose from the Si^{2+} ion irradiation. The results suggest a very significant effect of ion mass on the structural modification of the nanocluster films. Consistent with the data in Figure 5, phase transition of the

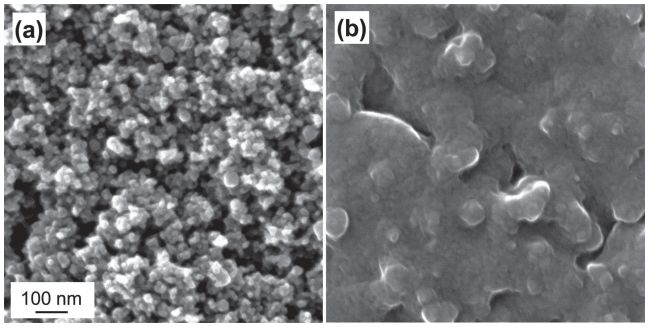

Figure 7. HIM micrographs of the same sample in Figure 6: (a) before and (b) after 5.5 MeV Si^{2+} ion irradiation to 1.5×10^{15} Si^{2+}/cm^2 (0.08 dpa at the surface) at nominally RT. The images have the same scalar bar and show a dramatic change in the nanostructure.

oxide shell from cubic magnetite Fe_3O_4 to cubic wüstite FeO is evident, as shown in **Figure 8**, where micro-beam GIXRD was used to eliminate interfering diffraction peaks from the Cu/Ti electrodes and Ag paste on the in situ sample. Data analysis from the whole-pattern fitting reveals that the average grain size increases from 5.3 to 9.4 nm for the Fe core and from 4.8 nm for the Fe_3O_4 shell to 5.5 nm for FeO shell after the Si^{2+} ion irradiation to 0.09 dpa. Except for the size variations that depend on the initial cluster states (e.g., size) and irradiation conditions (e.g., dose), there is an overall agreement on the irradiation behavior of the core-shell films shown in Figure 8 and 5.

Figure 9 shows the resistance data for a Fe-Fe_3O_4 core-shell nanocluster film irradiated with 5.5 MeV Si^{2+} ions at a higher temperature of 473 K. Thermal annealing of the film was conducted in vacuum at the elevated temperature for an extended time prior to ion irradiation and in situ resistance measurement. An initial rapid decrease followed by nearly invariance in resistance was observed during the thermal annealing process in the absence of ion irradiation. The in situ result shown in Figure 9 indicates that the resistance also has a super-exponential decay dependence on dose up to 0.21 dpa, similar to that from irradiation at nominally RT (Figure 6). However, irradiation of the annealed sample leads to a relatively smaller slope in the low-dose regime. A reduction of resistance by 80% from the initial value requires a dose of ~0.04 dpa at 473 K versus ~0.01 dpa at nominally RT. Again, the decrease in the electrical resistance of the nanocluster film is due to the grain growth

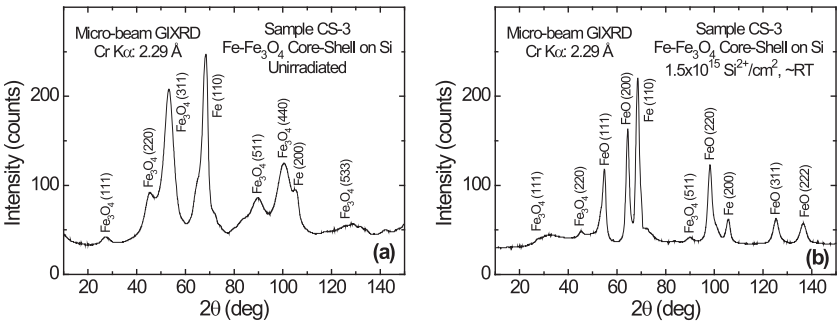

Figure 8. GIXRD patterns for the same sample in Figure 6: (a) before and (b) after 5.5 MeV Si^{2+} ion irradiation to 1.5×10^{15} Si^{2+}/cm^2 (0.09 dpa in the film) at nominally RT. A phase transition from cubic magnetite Fe_3O_4 to cubic wüstite FeO is observed.

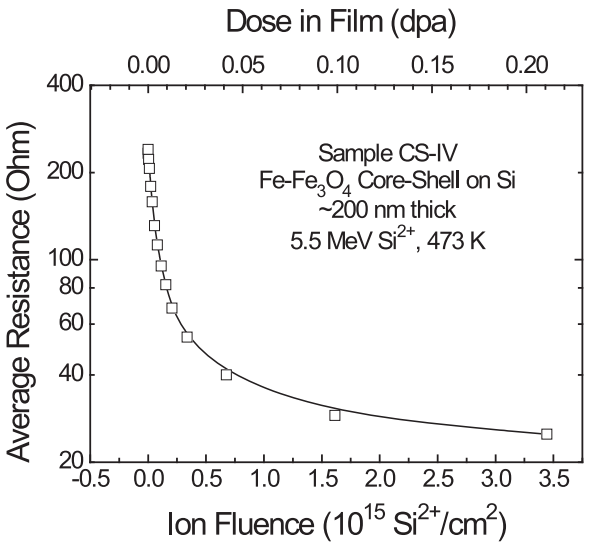

Figure 9. Electrical resistance of a Fe-Fe_3O_4 core-shell nanocluster film on surface-oxidized Si measured in situ using van der Pauw method as a function of ion fluence during 5.5 MeV Si^{2+} ion irradiation at 473 K. A super exponential decay behavior of the resistance is observed.

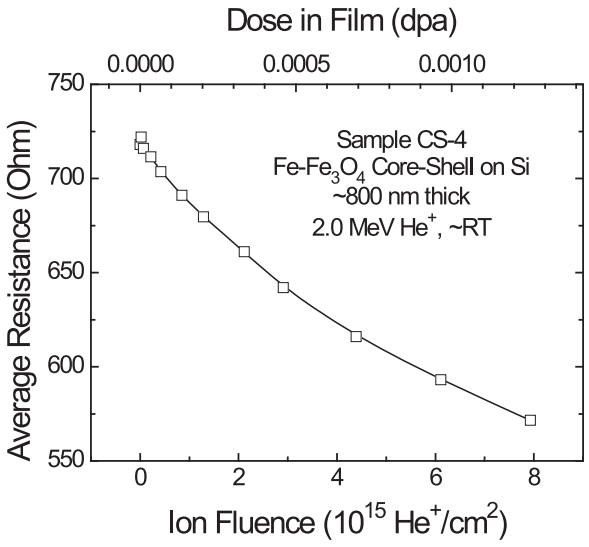

Figure 11. Electrical resistance of a Fe-Fe_3O_4 core-shell nanocluster film on surface-oxidized Si measured in situ using van der Pauw method as a function of ion fluence during 2.0 MeV He^+ ion irradiation at nominally RT. A significant decrease of the resistance is observed within a narrow dose window in the low-dose regime.

and a tighter connection between the agglomerated conducting particles, which leads to a larger effective cross-sectional area for more efficient electron transport. The corresponding surface nanostructure and diffraction pattern for the irradiated sample are shown in **Figure 10**. Interestingly, even at a higher dose, the nanostructure of the irradiated film at 473 K (Figure 10a) appears to be changed less dramatically than that irradiated at nominally RT (Figure 7b). There is also a noticeable difference in the shell, which does not undergo a phase transition to FeO at 473 K (Figure 10b). Compared to RT, the elevated temperature leads to a higher rate for simultaneous recombination of Frankel pairs created during ion irradiation, which should be responsible in part for more irradiation resistance of the Fe_3O_4 shell to structural modification and phase transition.

From Figure 6 and 9, the resistance changes in the low-dose regime are very rapid. A smaller step of dose was also applied to study the behavior quantitatively based on 2 MeV He^+ ion irradiation at a significantly lower dose rate. **Figure 11** shows the data for an 800 nm thick Fe-Fe_3O_4 nanocluster film; this thickness is small compared to the ion projected range of ~4 μm in the material under the irradiation conditions (Figure S1). At the highest applied ion fluence of 8×10^{15} He^+/cm^2, the corresponding dose in the film is only ~1.3×10^{-3} dpa. Figure 11 suggests that even at a dose as low as 10^{-3} dpa for He^+ ion irradiation at nominally RT, there is a considerable decrease in the resistance by ~15% in the Fe-Fe_3O_4 core-shell nanocluster film. However, at the highest dose applied to the film, a noticeable change in the surface nanostructure is not observed (Figure S3) and phase transition also does not occur (Figure S4). This is probably because the dose is still too low to produce any major visible effects on the nanostructure, yet quite significant on the electrical resistance already.

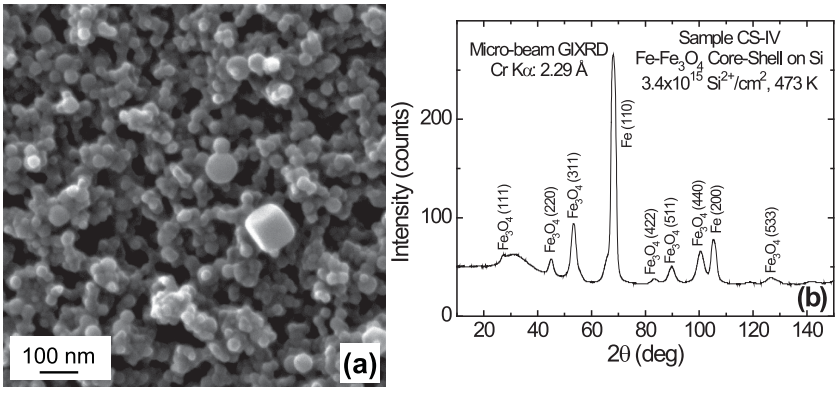

Figure 10. (a) HIM micrograph and (b) GIXRD pattern for the same sample in Figure 9 after 5.5 MeV Si^{2+} ion irradiation to 3.4×10^{15} Si^{2+}/cm^2 (~0.18 dpa at the surface and ~0.21 dpa in the film) at 473 K. Phase transition is not observed.

2.4. Future Studies

The nanocluster films used in this study has an inhomogeneous and anisotropic nature; their behavior of electrical resistance is complex under ion irradiation. Further studies are needed to better understand the basic mechanisms associated with the irradiation-induced microstructure changes, to develop an accurate interpretation to the observed dose dependence of the electrical resistance, and to establish the relationship between the nanostructural evolution and the super-exponential decay of the electrical resistance with dose. Meso-scale modeling will be performed and the results will be compared to the

experimental data to identify the dominant mechanisms in the structural evolution and its impact on the electrical resistance. The improved understanding, along with the verification of the material susceptibility to neutron irradiation, will help to lay a solid foundation for development of an advanced online, small neutron flux monitor based on nanocluster films as sensing materials.

3. Conclusions

It has been demonstrated that HIM provides a new capability for in situ study of nanostructural evolution on the surface of bulk materials under He^+ ion irradiation. Nanocluster films of Fe_3O_4 and Fe-Fe_3O_4 core-shells are found to undergo a dramatic change in nanostructure under ion irradiation. As dose increases, crystalline grains grow and nanoclusters aggregate, leading to formation of nanowire-like network along with nanopores. Phase transition of the oxide shell is observed from cubic magnetite Fe_3O_4 to cubic wüstite FeO. There are very significant effects of ion mass and irradiation temperature on structural modifications. The observed major nanostructural evolution is activated by elastic nuclear collisions that produce atomic displacements. Both electronic and thermal processes can play a significant role once the evolution is activated. In situ study of the nanocluster Fe-Fe_3O_4 films indicates that the electrical resistance has a super-exponential decay dependence on ion fluence or dose in dpa. The behavior has been attributed to the tighter interconnections between nanoparticles at higher doses, leading to an increase in the effective cross-sectional area for more efficient electron transport. The in situ results from this study provide physical insights into the processes involved in nanostructural evolution and changes in electrical resistance. The data also suggest that the nanocluster core-shell films may have great potential as candidate sensing materials for development of an advanced online neutron flux monitor with high detection sensitivity and long-term applicability at RT or elevated temperatures. These monitors would be of great value and importance in many nuclear operations to enhance safety, including those in existing and future nuclear power plants.

4. Experimental Section

Van der Pauw Sample Preparation (Figure S5): Si (100) substrates with an area of 10 mm × 10 mm and a SiO_2 surface layer of ~300 nm in thickness were used for van der Pauw sample preparation. To enhance adhesion strength between SiO_2 on the Si surface and electrode Cu, a Ti buffer layer (3 mm × 3 mm in area and 100 nm in thickness) was deposited onto the substrate in each of the four corners using a magnetron sputtering deposition system. Titanium layer has been known to be a good adhesive layer, particularly at the interfaces with Si or SiO_2.[38] Four Cu electrodes of 3 mm × 3 mm in area and 1 μm in thickness were deposited on the top of the Ti layers. Highly porous films of Fe_3O_4 or Fe-Fe_3O_4 core-shell nanoclusters with a dimension of about 5 mm × 5 mm were deposited at the center of the substrate with the four corners touching the Cu electrodes. A third-generation cluster-beam deposition system[39] was used for the nanocluster film deposition, which consists mainly of three components: a cluster source, a mass-selection chamber and a deposition chamber. Iron atoms from an ultra-high purity iron target sputtered by a high-pressure magnetron-sputtering gun are decelerated through their collisions with Ar gas injected continuously into the cluster growth chamber cooled by chilled water. Iron clusters are generated by Fe atomic interaction and condensation. The formed Fe clusters are ejected from a small nozzle by differential pumping. When oxygen gas is introduced into the source chamber or deposition chamber during processing, fully oxidized Fe clusters or uniform oxide shells on the core Fe clusters are formed prior to their soft landing onto the substrate near RT. The cluster size can be controlled to a narrow size distribution (5%) using the mass selector. Measurement of the film thickness was performed using in situ quartz crystal microbalance and ex situ 2.0 MeV He^+ Rutherford backscattering spectrometry (RBS) (based on 5.197 g/cm^3). Conducting Cu wires (0.14 mm in diameter) were bonded to each of the four Cu/Ti electrodes using PELCO high-performance silver paste (Product No. 16047).

In-Situ HIM Examination (Figure S6): A helium ion microscope (Orion Plus, Carl Zeiss SMT, Peabody, MA) was employed to investigate nanostructural evolution during He^+ ion irradiation. Irradiation of 25 or 30 keV He^+ ions was performed at nominally RT over a scanning area of 1 μm × 1 μm with 1024 × 1024 pixels at a dwelling time of 200 μs for each pixel. The beam current at the sample was reduced to typically 0.5 pA, leading to an ion flux of 3.1×10^{14} (He^+/cm^2)/s. The ion fluence for each image is taken as the arithmetic average of the initial and final fluences. Scans were repeated in the same area for 30 times to obtain consecutive image frames. Movies showing the nanostructural evolution as a function of ion fluence or dose in dpa at the surface were made from the image frames. The frames in the movie have been cropped in the same irradiated area to minimize sample drift effect for better visualization. Similar in situ study of the nanostructures was performed under 20 keV electron irradiation (at 0.96 nA over a scanning area of 2.5 μm × 2.3 μm) using a FIB/SEM system (FEI Quanta 3D FEG).

In Situ Resistance Measurement (Figure S7): Ion irradiation was performed using a 3.0 MV electrostatic tandem ion accelerator (NEC 9SDH-2 pelletron, Middleton, WI). Cluster films were irradiated at normal incidence with 5.5 MeV Si^{2+} ions to a fluence up to 10^{16} Si^{2+}/cm^2 or 2.0 MeV He^+ ions up to 8×10^{15} He^+/cm^2 at nominally RT or 473 K. A beam rastering system was used to ensure uniform irradiation covering the entire film area of 5 mm × 5 mm. Typical ion flux was on the order of 0.01 (Si^{2+}/nm^2)/s and 0.01 (He^+/nm^2)/s. The increase of the sample temperature was less than 50 K during the ion irradiation. In situ electrical resistance measurement of the nanocluster films was conducted based on reciprocal van der Pauw four-probe method, where arithmetic average of the resistance was obtained from two reversed polarity measurements. After each irradiation dose, a measurement was followed with beam off. The irradiation and measurement were conducted intermittently. In all events, ion energy was selected to be high enough to penetrate the films, leaving negligible amounts of implanted ions in the films.

XRD Analysis: The crystal structures of nanocluster films without electrodes before and after ion irradiation were analyzed using the Philips X'pert Multi-Purpose Diffractometer (MPD, PANalytical, Almelo, The Netherlands) based on fixed Cu Kα radiation (λ = 0.154187 nm). GIXRD was employed to study the crystallographic phase and average size of the crystalline grains at RT. This technique eliminates the strong diffraction peaks from the single-crystal substrate. In addition, to eliminate interfering diffraction peaks from the Cu/Ti electrodes and Ag paste, in situ samples were analyzed with micro-beam GIXRD on the nanocluster film. The data were collected using a Rigaku D/Max Rapid II instrument with a 2D image plate detector. X-rays were generated with a MicroMax 007HF generator fitted with a rotating Cr anode (λ = 0.22897 nm), focused on the specimen through a 300 mm diameter collimator. The samples were secured onto a flat reflection sample holder and fitted onto the sample stage. 2DP, Rigaku 2D Data Processing Software (version 1.0, Rigaku, 2007) was used to integrate the diffraction rings captured by the 2D image plate detector. The analysis of diffraction data was carried out using JADE 9.5.1 (Materials Data Inc.), TOPAS 4.2 (Bruker AXS GmbH, Karlsruhe, Germany), and PDF4+ 2012 database (ICSD).

Supporting Information

Supporting Information is available from the Wiley Online Library or from the author.

Acknowledgements

This study was supported by Laboratory Directed Research and Development at Pacific Northwest National Laboratory, operated by Battelle Memorial Institute for the US Department of Energy under Contract DE-AC05–76RL01830. A portion of the research was performed using EMSL, a national scientific user facility sponsored by the DOE's Office of Biological and Environmental Research and located at PNNL. Sample preparation was accomplished at the University of Idaho. WJ thanks Bruce Arey and Isaac Carroll at PNNL for performing the SEM experiment and Bill Thompson at Carl Zeiss SMT Inc. for valuable discussion.

Received: February 17, 2014
Revised: May 7, 2014
Published online: August 11, 2014

[1] C. D. Ferguson, L. E. Marburger, J. Doyne Farmer, A. Makhijani, *Nature* **2010**, *467*, 391.
[2] a) Y. Guérin, G. S. Was, S. J. Zinkle, *MRS Bull.* **2009**, *34*, 10; b) C. Ferguson, *Nature* **2011**, *471*, 411.
[3] P. C. Burns, R. C. Ewing, A. Navrotsky, *Science* **2012**, *335*, 1184.
[4] a) D. A. Clayton, R. T. Wood, *Nuclear News* **2011**, *54*(13), 42; b) S. Chu, A. Majumdar, *Nature* **2012**, *488*, 294.
[5] F. Murtas, G. Croci, A. Pietropaolo, G. Claps, C. D. Frost, E. Perelli Cippo, D. Raspino, M. Rebai, N. J. Rhodes, E. M. Schooneveld, M. Tardocchi, G. Gorini, *J. Instrum.* **2012**, *7*, p07021.
[6] P. Filliatre, C. Jammes, L. Oriol, B. Geslot, L. Vermeeren, *Proc. 1st Int. Conf. Advancements in Nuclear Instrumentation, Measurement Methods and Their Applications (ANIMMA)*, Marseille, France, **2009**, p. 1.
[7] L. Birstein, P. Martinez, A. Filevich, F. Li, *Nucl. Instr. Meth.* **1974**, *116*, 615.
[8] S. Bishnoi, T. Patel, M. Shukla, P. S. Adhikari, A. Sinha, *Proc. DAE Symp. Nucl. Phys.* **2012**, *57*, 880.
[9] D. Mouhssine, A. Nourreddine, A. Nachab, A. Pape, F. Fernandez, *Nucl. Instr. Meth. Phys. Res. B* **2005**, *227*, 609.
[10] a) A. S. Aricò, P. Bruce, B. Scrosati, J.-M. Tarascon, W. Van Schalkwijk, *Nat. Mater.* **2005**, *4*, 366; b) W. Jiang, W. J. Weber, C. M. Wang, J. S. Young, L. A. Boatner, J. Lian, L. M. Wang, R. C. Ewing, *Adv. Mater.* **2005**, *17*, 1602; c) G. Wang, X. Sun, F. Lu, H. Sun, M. Yu, W. Jiang, C. Liu, J. Lian, *Small* **2012**, *3*, 452.
[11] W. Jiang, J. S. McCloy, A. S. Lea, J. A. Sundararajan, Q. Yao, Y. Qiang, *Phys. Rev. B* **2011**, *83*, 134435.
[12] O. Akdogan, W. Li, B. Balasubramanian, D. J. Sellmyer, G. C. Hadjipanayis, *Adv. Funct. Mater.* **2013**, *23*, 3262.
[13] J. S. McCloy, W. Jiang, T. C. Droubay, T. Varga, L. Kovarik, J. A. Sundararajan, M. Kauer, Y. Qiang, E. C. Burks, K. Liu, *J. Appl. Phys.* **2013**, *114*, 083903.
[14] J. A. Hinks, *Nucl. Instrum. Meth. Phys. Res. A* **2009**, *267*, 3652.
[15] R. C. Birtcher, M. A. Kirk, K. Furuya, G. R. Lumpkin, M.-O. Ruault, *J. Mater. Res.* **2005**, *20*, 1654.
[16] K. Furuya, K. Mitsuishi, M. Song, T. Saito, *J. Electron Micros.* **1999**, *48*, 511.
[17] P. Trocellier, Y. Serruys, S. Miro, E. Bordas, S. Pellegrino, S. Vaubaillon, M. O. Ruault, S. Henry, O. Kaïtasov, *Nucl. Instrum. Meth. Phys. Res. B* **2008**, *266*, 3178.
[18] L. P. Guo, C. S. Liu, M. Li, B. Song, M. S. Ye, D. J. Fu, X. J. Fan, *Nucl. Instrum. Meth. Phys. Res. A* **2008**, *586*, 143.
[19] P. Hosemann, *Rev. Accelerator Sci. Tech.* **2011**, *4*, 161.
[20] M.-O. Ruaylt, F. Fortuna, H. Bernas, J. Chaumont, O. Kaïtasov, V. A. Borodin, *J. Mater. Res.* **2005**, *20*, 1654.
[21] a) J. Y. Huang, L. Zhong, C. M. Wang, J. P. Sullivan, W. Xu, L. Q. Zhang, S. X. Mao, N. S. Hudak, X. H. Liu, A. Subramanian, H. Fan, L. Qi, A. Kushima, J. Li, *Science* **2010**, *330*, 1515; b) K.-W. Nam, S.-M. Bak, E. Hu, X. Yu, Y. Zhou, X. Wang, L. Wu, Y. Zhu, K.-Y. Chung, X.-Q. Yang, *Adv. Funct. Mater.* **2013**, *23*, 1047; c) X. Tao, J. Du, Y. Sun, S. Zhou, Y. Xia, H. Huang, Y. Gan, W. Zhang, X. Li, *Adv. Funct. Mater.* **2013**, *23*, 4745; d) M. Gu, L. R. Parent, B. L. Mehdi, R. R. Unocic, M. T. McDowell, R. L. Sacci, W. Xu, J. G. Connell, P. Xu, P. Abellan, X. Chen, Y. Zhang, D. E. Perea, J. E. Evans, L. J. Lauhon, J.-G. Zhang, J. Liu, N. D. Browning, Y. Cui, I. Arslan, C. M. Wang, *Nano Lett.* **2013**, *13*, 6106.
[22] a) J. Morgan, J. Notte, R. Hill, B. Ward, *Microsc. Today* **2006**, *14*, 24; b) M. Ananth, L. Scipioni, J. Notte, *Am. Lab.* **2008**, *40*, 42; c) L. Scipioni, L. A. Stern, J. Notte, S. Sijbrandij, B. Griffin, *Adv. Mater. Process.* **2008**, *166*, 27; d) R. Hill, J. A. Notte, L. Scipioni, *Advances in Imaging and Electron Physics* (Edited by P. W. Hawkes) Elsevier Inc., Amsterdam, **2012**, p.p. 65–148.
[23] a) D. C. Bell, M. C. Lemme, L. A. Stern, J. R. Williams, C. M. Marcus, *Nanotechnology* **2009**, *20*, 455301; b) M. C. Lemme, D. C. Bell, J. R. Williams, L. A. Stern, B. W. H. Baugher, P. J. Herrero, C. M. Marcus, *ACS Nano* **2009**, *3*, 2674.
[24] a) M. T. Postek, A. E. Vladár, *Scanning* **2008**, *30*, 457; b) B. P. Danysh, T. P. Patel, K. J. Czymmek, D. A. Edwards, L. Wang, J. Pande, M. K. Duncan, *Matrix Biology* **2010**, *29*, 228; c) W. Jiang, R. Devanathan, C. J. Sundgren, M. Ishimaru, K. Sato, T. Varga, S. Manandhar, A. Benyagoub, *Acta Mater.* **2013**, *61*, 7904.
[25] V. Sidorkin, E. van Veldhoven, E. van der Drift, P. Alkemade, H. Salemink, D. Maas, *J. Vac. Sci. Tech. B* **2009**, *27*, L18.
[26] S. Sijbrandij, B. Thompson, J. Notte, B. W. Ward, N. P. Economou, *J. Vac. Sci. Sci. Technol. B* **2008**, *26*, 2103.
[27] R. Livengood, S. Tan, Y. Greenzweig, J. Notte, S. McVey, *J. Vac. Sci. Technol. B* **2009**, *27*, 3244.
[28] a) L. J. Van der Pauw, *Philips Research Reports* **1958**, *13*, 1; b) L. J. Van der Pauw, *Philips Tech. Rev.* **1958**, *20*, 220.
[29] G. J. Dienes, *Annu. Rev. Nucl. Sci.* **1953**, *2*, 187.
[30] J. F. Ziegler, J. P. Biersack, U. Littmark, *The Stopping and Range of Ions in Solids*, Pergamon, New York, **1985**; available at: http://www.srim.org.
[31] M. N. Özişik, *Boundary Value Problems of Heat Conduction*, Dover Publications, Inc., Mineola, New York, **2002**, p. 311.
[32] a) S. J. Zinkle, C. Kinoshita, *J. Nucl. Mater.* **1997**, *251*, 200; b) E. A. kotomin, A. I. Popov, *Nucl. Instrum. Meth. Phys. Res. B* **1998**, *141*, 1.
[33] M. J. Berger, J. S. Coursey, M. A. Zuker, J. Chang, *Stopping Power and Range Tables for Electrons, Protons, and Helium Ions*, December 9, 2011. Available at: http://www.nist.gov/pml/data/star/index.cfm.
[34] W. H. Bragg, R. Kleeman, *Philos. Mag.* **1905**, *10*, S318.
[35] R. F. C. Farrow, P. M. Rice, M. F. Toney, R. F. Marks, J. A. Hedstrom, R. Stephenson, M. J. Carey, A. J. Kellock, *J. Appl. Phys.* **2003**, *93*, 5626.
[36] Z. Fang, K. Terakura, H. Sawada, T. Miyazaki, I. Solovyev, *Phys. Rev. Lett.* **1998**, *81*, 1027.
[37] A. J. Pignocco, G. E. Pellissier, *J. Electrochem Soc.* **1965**, *112*, 1188.
[38] a) I. P. Koutsaroffa, M. Zelnera, P. Wooa, L. Mcneila, M. Buchbindera, A. Cervin-Lawrya, *Integrated Ferroelectrics* **2002**, *45*, 97; b) Y. K. Ko, S. Lee, H. M. Lee, H. J. Yang, J. Y. Kim, J. Kim, J. H. Lee, H. J. Shin, W. J. Nam, J. G. Lee, *J. Kor. Phys. Soc.* **2005**, *47*, S467; c) B. Lahiri, R. Dylewicz, R. M. D. L. Rue, N. P. Johnson, *Opt. Express* **2010**, *18*, 11202.
[39] a) Y. Qiang, J. Antony, A. Sharma, J. Nutting, D. Sikes, D. Meyer, *J. Nanoparticle Res.* **2006**, *8*, 489; b) M. Kaur, J. S. McCloy, W. Jiang, Q. Yao, Y. Qiang, *J. Phys. Chem. C* **2012**, *116*, 12875.